

Evaluation of a Microreactor for Flow Biocatalysis by Combined Theory and Experiment

Teresa Burgahn,^[a] Philip Pietrek,^[b] Roland Dittmeyer,^[b] Kersten S. Rabe,^[a] and Christof M. Niemeyer*^[a]

The operation of enzyme cascades in microfluidic devices is a current field of research that promises manifold applications in biocatalysis. For an optimization of flow biocatalysis systems it is desirable to model the reactor *in silico* in order to enable a better understanding and thus an economic optimization of the reaction systems. However, due to their high complexity, it is still difficult to simulate coupled enzyme reactions. We here describe a new model for a plug flow reactor consisting of a

porous bed of compact uniform particles functionalized with an immobilized ketoreductase (Gre2) which is overflowed by a mobile phase containing the enzymatic NADPH cofactor regeneration system based on glucose dehydrogenase (GDH). By studying different flow rates, lengths and layer thicknesses of the catalytic bed, we show that the synergy of experiment and mathematical modeling can optimize the space-time yields of the reaction system.

1. Introduction

Chemical synthesis of complex organic molecules for drug development has benefited immensely from recent developments in flow chemistry and automation.^[1] In this respect, the use of microfluidic devices is highly advantageous as it simplifies the precise adjustment and control of essential reaction parameters, such as temperature and diffusion-based mixing efficacy, and it also allows the separation of incompatible reaction steps.^[2] In this area of research, the spatial compartmentalization and cascading of reaction steps are increasingly exploited for chemical transformations in microfluidic reactors.^[3] Here the synthesis of drugs with multiple stereocenters is a prime example of how cascaded biocatalytic^[4] or chemoenzymatic^[5] reaction sequences can be used for efficient, scalable production processes.^[6]

For effective implementation of continuous flow processes, however, the integration of biocatalysts into microfluidic devices is still a major challenge.^[7] The immobilization of whole cells or isolated enzymes can be achieved by a plethora of methods, ranging from non-specific physisorption to the use of

sophisticated chemical methods, which are often based on genetically-encoded tag systems, such as the (His₆)-tag.^[8] Likewise, tag systems used for purification, e.g., streptavidin-binding peptide (SBP),^[9] or cell biology research (e.g., SpyTag/SpyCatcher,^[10] SNAP-Tag,^[11] HaloTag^[12]) are being exploited for flow-through biocatalysis. Indeed, the use of fusion proteins decorated with such tag systems has led to the establishment of 'self-immobilizing biocatalysts' that can be used in continuous microfluidic processes with high efficiency and specificity.^[13] The self-assembled immobilization of such fusion proteins can, for example, be achieved on magnetic beads with a high level of control over stoichiometry and geometric alignment by single-point immobilization.^[14] The further integration of such enzyme-functionalized magnetic nano- and microparticles into flow-through reactors enables a variety of applications, ranging from sensors^[15] and lab-on-a-chip systems^[16] to continuous flow-through reactors for biocatalysis.^[13a,b,17]

The use of immobilized enzymes in flow-through systems allows the biocatalysis process to be carried out in a heterogeneous catalysis regime, often in a packed-bed reactor format. For an optimization of such systems, it would be desirable to model the process *in silico*, in order to gain a better understanding of the biotechnological process and to enable its economic optimization with reduced experiments and resources. However, it is still difficult to describe and simulate coupled enzyme reactions that occur in a microfluidic setup with an overflowed, porous, catalytically active bed due to the high complexity of such systems.

The detailed simulation of the reactor performance in such a system requires mathematical models for the enzymatic processes, which depend on kinetic models for the distinctive chemical conversions. Mathematical descriptions of enzyme kinetics, in particular Michaelis and Menten kinetics,^[18] have led to the range of today's methodologies, such as canonical, approximate and mechanistic rate formalisms.^[19] However, Michaelis-Menten kinetics assumes constant, excess concentrations of co-substrates, and these conditions are usually not

[a] T. Burgahn, Dr. K. S. Rabe, Prof. C. M. Niemeyer
Karlsruhe Institute of Technology (KIT)
Institute for Biological Interfaces (IBG 1)
Hermann-von-Helmholtz-Platz 1
D-76344 Eggenstein-Leopoldshafen (Germany)
Telefax: +49 (0)721-608-2-5546
E-mail: niemeyer@kit.edu

[b] P. Pietrek, Prof. R. Dittmeyer
Karlsruhe Institute of Technology (KIT)
Institute for Micro Process Engineering (IMVT)
Hermann-von-Helmholtz-Platz 1
D-76344 Eggenstein-Leopoldshafen (Germany)

Supporting information for this article is available on the WWW under <https://doi.org/10.1002/cctc.202000145>

© 2020 The Authors. Published by Wiley-VCH Verlag GmbH & Co. KGaA. This is an open access article under the terms of the Creative Commons Attribution Non-Commercial NoDerivs License, which permits use and distribution in any medium, provided the original work is properly cited, the use is non-commercial and no modifications or adaptations are made.

present inside microfluidic packed-bed reactors. For instance, Lilly *et al.* found decreased Michaelis-Menten K_m values for increased flow rates and therefore made estimations on enzyme kinetic parameters in continuous-flow systems.^[20] In addition, for enzymes using two substrates, multi-substrate laws such as *bi-bi* mechanisms must be considered, which are divided into sequential mechanisms (ordered or random binding) and the ping-pong mechanism.^[21]

In order to implement such mechanistic reaction kinetics into packed-bed reactors containing porous particles, several mathematical models have been developed in earlier works.^[22] However, these works focused on investigations of packed bed reactors with particle diameters larger than 300 μm operated by perfusion through the packed bed. To expand this methodological repertoire to complex, multi-substrate enzymatic reactions, we here describe a new model for a plug flow reactor consisting of a porous bed of compact, uniform particles functionalized with an immobilized reductase which is overflowed with an aqueous mobile phase containing an enzymatic NADPH cofactor regeneration system. We show that through the synergy of experiment and mathematical modeling, the behavior of the reaction system can be predicted, thereby reducing the number of experiments as well as the material consumption for optimizing the catalytic performance of the system.

2. Microreactor and mathematical model

2.1. Reactor model

In this work we utilize a previously reported reaction system employing a ketoreductase enzyme immobilized on magnetic beads (MB) in a microreactor.^[13a] The microfluidic reactor contains uniform enzyme-functionalized MBs with a diameter of 2.8 μm that are located inside a straight channel of a poly (methylmethacrylate) (PMMA) chip (58.5 \times 1 \times 0.2 mm, length \times width \times height). The MBs form a packed layer inside the reactor and are kept in place by magnets underneath the chip. Constant temperature of the system is applied by using a heated chipholder. The substrate, co-substrate, cofactors and a cofactor regeneration enzyme are continuously fed to the reactor system via a solution flowing over the MB layer. A detailed illustration of the reactor is given in Figure S1, Supporting Information.

To acquire a detailed understanding of the system and its possible limitations, the reactor setup was translated into a mathematical model in Matlab. The reactor is modeled as a 1D cascade of segments in flow direction. Each segment contains a whole channel cross-section with identical predefined length and is assumed to consist of a porous catalyst layer with a volume V_{bed} formed by the MBs attached to the bottom wall, in addition to a well-mixed free volume V_{ec} above that layer (Figure 1). The model assumes that the reaction rates and concentrations are constant and do not change over the width of the channel (z -axis), thus reducing the simulation to the x -axis in flow direction and the y -axis (channel height).

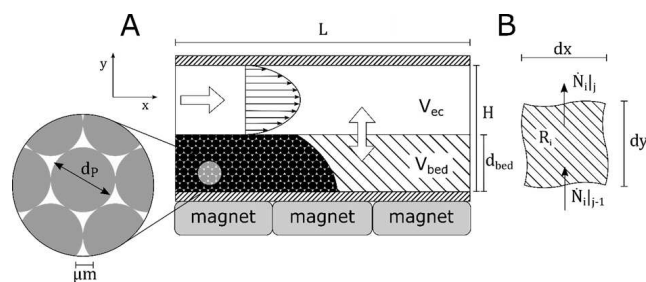


Figure 1. Flow Reactor. A) 2D Schematic illustration of the reactor for the middle of the channel and the governing mass transport processes. B) Infinitesimal volume inside the packed MB layer with mass transport and source term.

Figure 1 A shows an idealized 2D representation of the reactor with the visualized velocity profile representing the profile in the center of the channel. The actual velocity profile of the liquid could deviate from the ideal symmetrical flow profile due to changes in the roughness, contact angle and surface polarity of the packed bed surface, which differs from that of the rectangular walls. Furthermore, secondary flows might occur at the edges of the rectangular channel. These processes might influence the velocity of volume elements near the interfaces and even lead to a transition from a laminar to a turbulent flow regime near the walls.^[23] Turbulence at the packed bed/liquid volume interface would increase mixing and mass transport to and from the reactive layer, reducing the boundary layer and creating a steeper velocity profile. While these processes might be taken into account in further refinements of the model, they were neglected here because the low flow rates (0.5–2 $\mu\text{L}/\text{min}$) applied in this study result in very low Reynolds numbers ($Re < 1$), thereby minimizing turbulences at the top of the MB layer.

Due to the compact packing of the MBs (discussed below), perfusion through the bed of the reactor is negligible and, thus, the model disregards convective flow within the packed bed in flow direction. Transport in the free volume takes place as a constant flow from one segment to the next. By choosing a sufficiently small size (or a sufficiently large number) of segments, the axial back diffusion can be neglected and an ideal mixing in the segments can be assumed. The expected number of segments can be derived from the Bodenstein number $Bo = \frac{uL}{D_{ax}}$ according to $N = \frac{Bo}{2}$, where D_{ax} is the axial dispersion coefficient.^[24] To account for uncertainties from turbulences and increased mixing, we used a high number of 250 segments that were calculated for a laminar flow regime to simulate an ideal mixing behavior in each segment. The axial diffusion within the layer was not taken into account in the model (Figure 1B).

The model assumes a finite mass transfer between the packed bed and the free volume. This is addressed by the Sherwood correlation for wall mass transfer in rectangular micro channels formulated by Kockmann.^[25] This correlation was derived with respect to the governed flow regime for a porous catalytic layer that differs from the MB layer. While the current work is based on the idealized correlation, the model could be

improved in future work by empirical investigation of the mass transfer behavior of the MB layer to derive a modified Sherwood correlation.

Chemical reactions are catalyzed by the enzymes immobilized on the MBs (Gre2, see below) as well as by the dissolved enzymes (GDH) in the homogeneous solution of the mobile phase. Hence, for an infinitesimal volume (see Figure 1B) in the MB layer the following material balance equation holds:

$$\frac{dN_i}{dt} \Big|_j = \dot{N}_i \Big|_{j-1} - \dot{N}_i \Big|_j + R_i dV \quad (1)$$

$$dV \frac{dc_i}{dt} = D_{i,e} \left(\frac{\partial c_i}{\partial y} \Big|_{j-1} - \frac{\partial c_i}{\partial y} \Big|_j \right) dx \cdot W + R_i dV \quad (2)$$

With N_i and describing the amount and flow of component i . This describes the change in concentration of a component i inside a pseudo-homogeneous volume $dV = dx \cdot dy \cdot W$ with $D_{i,e}$ representing the effective diffusivity of component i in the packed MB layer and $R_i = f(c_i)$ the local pseudo-homogeneous reaction rate which depends on the concentration. dx and dy are the two dimensions of an infinitesimal volume in x and y direction, whereas W is the width of the channel. Since the temperature of the system was kept constant all physical and transport properties were considered constant as well.

To estimate the complex diffusion behavior inside the MB layer we calculated the molecular diffusion coefficients D_i according to Wilke and Chang for dilute solutions in water (see also Materials and Methods, S1).^[26] The resulting values are listed in Table S2. In order to take into account that the porous MB layer affects the diffusion, the process is described as the diffusion through a cylindrical pore. The ratio between pore volume and total volume is defined as porosity ε_{bed} , whereas the shape and curvature of the pore is given by the tortuosity τ_{bed} . The effective diffusion coefficient of a component i is given by $D_{i,e} = D_i \frac{\varepsilon_{bed}}{\tau_{bed}}$.^[27] In order to determine the GDH concentration inside the packed reactor bed, calculations for a flow rate of 0.5 $\mu\text{L}/\text{min}$ were performed. The calculations indicated that the GDH is evenly distributed inside the bed after 3000 seconds (Figure S2). Hence, since the outflow of the reactor was analyzed after reaction times of >1 hour, a constant GDH concentration in the entire microreactor was assumed at the time of sampling.

As a result of the strong magnetic forces holding the MBs inside the reactor, an ideal homogenous cubic close packing was assumed ($\varepsilon_{bed} = 0.259$). We thus calculated the porosity and tortuosity using appropriate correlations describing the MB layer ($\varepsilon_{bed} = 0.27$ $\tau_{bed} = 1.68$).^[28] This value was calculated from a filled channel (4.5 mg MBs with a mean density of 1.4 g/cm^3 and a diameter of 2.8 μm). However experimental analysis revealed slight inhomogeneities of the particle layer, e.g. grooves, presumably formed by magnetic interactions between the particles and the holder magnets (Figure S3 A). To roughly estimate the impact of these topological inhomogeneities, we assumed that the entire bed consists of columns of porous bed volumes of MBs alternating with empty reactor space of identical volume. This drastic assumption would increase the

mean diffusion in the bed volume by a factor of 3.7 and result in only a minimal 1% increase in conversion of the substrate 1.

With the assumption of steady state and Taylor approximation, eq. (2) reduces to the following differential equation, where R_i represents the concentration dependent source term of component i .

$$0 = D_{i,e} \cdot \frac{d^2 c_i}{dy^2} + R_i \quad (3)$$

Solving this 2nd order ordinary differential equation requires the definition of two boundary conditions per chemical species. A Neumann condition is used at the bottom and at the top of the packed-bed, connecting V_{ec} and V_{bed} in each segment.

$$\text{bottom: } \frac{dc_i}{dy} \Big|_{y=0} = 0 \quad \text{top: } \frac{dc_i}{dy} \Big|_{y=d_{bed}} = \frac{k_L}{D_{i,e}} (c_{i,out} - c_i \Big|_{y=d_{bed}}) \quad (4)$$

The mass transfer coefficient $k_L = (1/\beta_i)^{-1}$ is calculated with the previously described Sherwood Correlation to derive the Sherwood number $Sh = \frac{\beta_i d_h}{D_i}$. To determine the unknown species concentrations $c_{i,out}$ the component material balance for the well-mixed free channel volume V_{ec} is introduced:

$$0 = u_f (c_{i,in} - c_{i,out}) (H - d_{bed}) + k_L (c_{i,out} - c_i \Big|_{y=d_{bed}}) \Delta x + R_i \Delta x (H - d_{bed}) \quad (5)$$

Eq. 5 connects the reactor segments by implementing incoming and outflowing substance i flows. Inlet concentrations, flow rates, enzyme concentrations and other reactor parameters are set according to the experimental conditions.

2.2. Reaction network

In order to provide detailed experimentally determined kinetic parameters for the mathematical models we used a previously established modular reaction system for the (*S*)-selective reduction of the symmetrical diketone 5-nitrononane-2,8-dione 1 by the (*S*)-selective methylglyoxal reductase Gre2 using glucose 1-dehydrogenase GDH for NADPH cofactor regeneration (Figure 2).^[13a,29] Due to the prostereogenic carbon atom in the mirror plane of 1 a single reduction step can form four stereoisomeric hydroxyketones. While we have previously

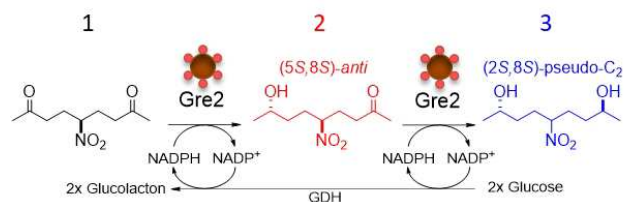


Figure 2. Reaction Network. Reduction of the educt 5-nitrononane-2,8-dione (NDK) 1 by the (*S*)-enantioselective ketoreductase Gre2 yields exclusively one stereoisomer of the hydroxyketone 2 (red), which can be further reduced to the shown isomer of diol 3 (blue).^[13a] For both reactions, NADPH is provided by GDH-mediated cofactor regeneration in the mobile phase of the reactor.

shown that all of these isomers can be produced with appropriate (*S*)- and (*R*)-selective ketoreductase enzymes, we here employed the most selective enzyme, Gre2, that exclusively forms one (5*S*, 8*S*)-anti-configured stereoisomer of the hydroxyketone **2** (red, Figure 2). At high enzyme concentrations, **2** can be further reduced to selectively produce one (2*S*, 8*S*)-pseudo-*C*₂-configured diol **3** (blue), however with a substantially lower reaction rate.^[13a,29] Notably, no indication of inhibitory effects was observed in our previous studies. To operate the enzyme in a packed-bed microreactor format, we used a variant of Gre2 that is genetically fused to a self-immobilizing Halo-tag variant and displays the same reaction properties as the native Gre2.^[13a]

2.3. Kinetic modelling

Implementing this reaction network in the above described reactor model requires biochemical kinetic rate laws to describe the occurring reactions. By considering molecular association, biochemical conversion and dissociation processes, Liebermeister *et al.* created modular rate laws and generalized mathematical formulations to describe these processes, depending on the prevailing mechanisms.^[30] In deriving these mathematical descriptions of enzymatic reactions, the following mechanisms were assumed: (i) sequential binding and dissociation of the reactants, (ii) the binding of the reactants is reversible and much faster than the catalytic step (fast equilibrium assumption) and (iii) the binding energies of the individual reactants do not depend on other reactants already bound to the enzyme.^[31] These formulations can be easily implemented in the modeling due to the reduced number of kinetic parameters, a consistent thermodynamic constraint and the high flexibility with respect to enzymatic mechanisms.



For a *bi-bi* reaction according to eq. (6) the rate laws are defined by:

$$v_r = c_E \cdot \frac{T_r}{(D_r^{reg} + D_r)} \quad (7)$$

With

$$T_r = k_{cat}^+ \frac{c_A c_B}{K_M^A K_M^B} - k^- \frac{c_P c_Q}{K_M^P K_M^Q} \quad (8)$$

The numerator T_r provides an option for reversible and irreversible reactions, and contains the concentrations of reactants and products as well as the Michaelis-Menten or association constants for each component. The term D_r^{reg} addresses kinetic effects such as inhibition or activation of the reaction (eq. (9)). We extended the formulated generalized kinetics based on sequential mechanism (common modular) of Liebermeister *et al.*^[30] to cover as well the ping-pong mechanisms (eq. 12). In order to determine the kinetic parameters of both enzymes we assumed the reduction reactions as irrever-

sible and the cofactor regeneration as reversible.^[13a] Based on earlier works on the catalytic mechanism of Gre2^[33] and GDH^[34] *bi-bi* reaction mechanisms were assumed for both reactions also taking into account possible limitations due to mass transport, i.e. low concentrations of both educts. As investigated by Guo *et al.*,^[33] a sequential ordered mechanism was considered for the Gre2 reduction reaction. Although earlier work did not provide any evidence of product inhibition,^[13a] inhibitory effects of **2** and **3** were taken into account in the simulation to reflect the fact that **1**, **2** and **3** share the same binding pocket (see Table S3).

Due to the lack of knowledge about the exact mechanism of GDH, we initially considered both the ping-pong and sequential mechanism for the kinetic model. A distinction between a random and an ordered sequential mechanism was not necessary, because there is no indication of inhibitory reactions for the cofactor regeneration reaction.

Depending on the mechanism, the denominator D_r is adjusted as indicated by equations (10)–(12). For being consistent with thermodynamics and mass conservation, rate laws need to satisfy Haldane relationships and Wegscheider conditions.^[32] With these conditions the rate law was rewritten with a reduced number of independent kinetic parameters (see Supplementary Information).

$$D_r^{reg} = \sum_i \left(\frac{K_i^A}{c_i} \right) + \sum_i \left(\frac{K_i^B}{c_i} \right) \quad (9)$$

$$D_{r,rand} = \left(1 + \frac{c_A}{K_M^A} \right) \left(1 + \frac{c_B}{K_M^B} \right) + \left(1 + \frac{c_P}{K_M^P} \right) \left(1 + \frac{c_Q}{K_M^Q} \right) - 1 \quad (10)$$

$$D_{r,ord} = 1 + \frac{c_A}{K_M^A} + \frac{c_Q}{K_M^Q} + \frac{c_A c_Q}{K_M^A K_M^Q} + \frac{c_P}{K_M^P} + \frac{c_B}{K_M^B} + \frac{c_P c_B}{K_M^P K_M^B} + \frac{c_A c_P}{K_M^A K_M^P} + \frac{c_B c_Q}{K_M^B K_M^Q} + \frac{c_A c_P c_B}{K_M^A K_M^P K_M^B} + \frac{c_B c_P c_Q}{K_M^B K_M^P K_M^Q} \quad (11)$$

$$D_{r,PingPong} = \frac{c_A}{K_M^A} + \frac{c_B}{K_M^B} + \frac{c_P}{K_M^P} + \frac{c_Q}{K_M^Q} + \frac{c_A c_P}{K_M^A K_M^P} + \frac{c_B c_Q}{K_M^B K_M^Q} \quad (12)$$

3. Results and discussion

3.1. Kinetic behaviour of the reaction system

To establish a detailed model of the reactor, we experimentally characterized the enzymes in homogeneous solution by determining the enzymatic activities of Gre2 and GDH under assay conditions (Figure S4–S6). To exclude artifacts from competitive reactions, we also confirmed that GDH in the mobile phase is not competing for NADPH in the absence of the co-substrate glucose (Figure S7). Furthermore, we confirmed that the glucose/GDH regeneration system provides a constant NADPH concentration, even under steady-state equilibrium with Gre2 reductase activity (Figure S8). These experiments also revealed that the sequential mechanism showed a much better alignment with experimental data than the ping-pong mechanism (Figure S8). The sequential random mecha-

nism was thus applied for modeling of the GDH reaction. The initial reaction rates v_0 of the GDH for cofactor regeneration were analyzed for variable concentrations of glucose and NADP⁺ (Figure S9). These batch experiments allowed us, by fitting with a sequential mechanism, to determine the K_m and k_{cat} values of the enzymes in order to use them for reactor modeling.

For the determination of the kinetic behavior of the reduction reactions, initial reaction rates v_0 of Gre2 were determined by batch experiments for variable concentrations of substrate 1 (Figure S10) using either a fixed starting concentration of excess NADPH (0.5 mM, Figure S10 A) or constant cofactor concentration through enzymatic regeneration (Figure S10B). The data was fitted assuming a Michaelis-Menten mechanism. As expected, the results clearly indicated that provision of constantly high concentrations of NADPH, maintained by the cofactor regeneration system, leads to increased maximum reaction velocity V_{max} ($0.36 \pm 0.04 \mu\text{M}/\text{sec}$), as compared to the system lacking NADPH regeneration ($0.12 \pm 0.01 \mu\text{M}/\text{sec}$). However, both alternatives do not deliver a sufficiently high excess of NADPH (0.5 mM) over the substrate 1 (10 mM) to meet the demands of classical Michaelis-Menten kinetics. Likewise, while a Michaelis-Menten approach could be used to describe the enzymatic reactions in the batch experiments, in the more complex reaction system of the flow reactor, one has to take into account potential mass transport limitations inside the MB layer, which can lead to low educt concentrations. Furthermore, although Gre2 favors the reduction of 1, the second reduction step from 2 to 3 gets more relevant once the concentration of 1 drops (Figure S11). In such cases, Michaelis-Menten kinetics is not suited anymore. By taking into account earlier works on the catalytic mechanism of Gre2^[33] and GDH,^[34] we solved this problem by assuming the above described multisubstrate *bi-bi* reaction mechanisms for both enzyme reactions. As shown in Figure 3, the implementation of the multi-substrate mechanism in the modeling of the Gre2-catalyzed transformation of 1 led to a good agreement of the experimental data (Figure S10B) with the simulation.

The data of these experiments were fed in an idealized batch reactor model to perform a nonlinear parameter fit to determine the kinetic parameters k_{cat}^+ and K_m for both reduction reactions. Details of the simulation are summarized in the Supplementary Information and the obtained values are listed in Table S3. The catalytic constant k_{cat}^+ represents the enzymatic turnover rate of a substrate i and the association constant K_m indicates the affinity of substrate i to form an enzyme/substrate complex. Due to the two prochiral carbon atoms of 1, the probability to form a complex with the enzyme is greater than for 2, which is reflected in a larger K_m . NADP⁺ and NADPH have the same influence on both reductions, resulting in an identical association constant (see Table S3). The kinetic parameters for the soluble enzymes calculated from the data in Figure 3 and Figure S8–S11 were used as the starting values for the fitting of the corresponding parameters of the immobilized enzymes.

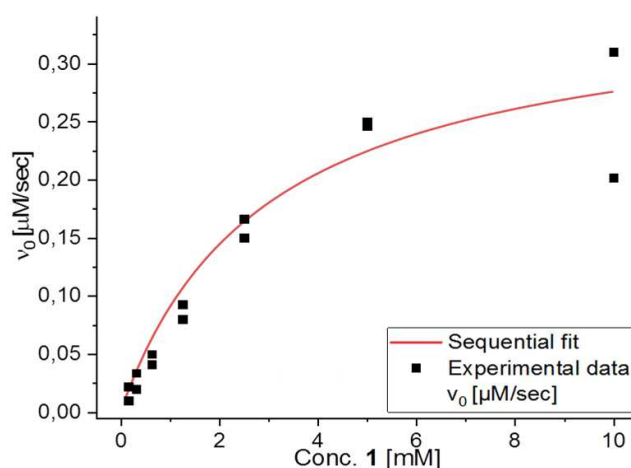


Figure 3. Simulation can predict the initial reaction rates for the reduction of 1 by Gre2 under cofactor regeneration conditions. Initial reaction velocities v_0 were determined using variable concentrations of 1 in the presence of constant amounts of NADPH provided by the GDH/glucose regeneration system (See Figure S10). A sequential mechanism was applied for both the Gre2 and the GDH reactions. The corresponding kinetic parameters are listed in Table S3.

3.2. Microfluidic studies

Gre2-functionalized MB (in the following denoted as Gre2-MBs) were used as catalytic entities in the flow reactor (Figure 1). For the immobilization of HOB-tagged Gre2 onto MB, commercially available streptavidin (STV)-coated MB were modified with the bifunctional linker Btn-PEG-CH to install chlorohexane (CH) groups on the beads. The CH groups enable covalent capture of the HOB domain (Figure S12). The Gre2-MBs were loaded into a straight channel microfluidic reactor made of PMMA, as previously described.^[13a] The full channel contained 4.5 mg of Gre2-MBs with an enzyme loading of $25.4 \pm 4.3 \text{ pmol Gre2 per mg MB}$, as determined by SDS-PAGE analysis (Figure S13). The magnetic particles were retained in the flow channel by eight Nd magnets, leading to formation of a packed particle bed at the bottom of the channel. The length of the particle bed obtained with 4.5 mg of Gre2-MBs was determined as 50 mm (in the following referred to as “1x”, see Figure S3 D). The morphology of the packed bed was analyzed by confocal fluorescence microscopy (Figure S3 A). Estimated from Z-stack analysis, the thickness of the bed was approximately 90 μm with a total channel height of 200 μm . This value, obtained with 4.5 mg of Gre2-MBs, is in the following referred to as “1x” thickness (see Figure S3 D). These 1x values were taken as reference dimensions of the packed-bed for the further variations.

By using the various parameters described above, we could now model the cofactor regeneration and improve the resulting kinetic parameters for immobilized Gre2 enzymes (given in Table S3) by fitting them to the experimental data. In order to collect comparable data, all experimental results in the following were obtained under steady-state conditions with an operation time of at least one hour. Results from the model are

given without deviations as no probability calculations were implemented in the simulation.

With the kinetic parameters from Table S3 at hand, investigation by experiment and simulation of different reactor geometries and operation conditions was now possible. We focused on the space-time yield (STY), which relates the yield of 2 to the space-time τ and was used as a measure for a production-oriented evaluation of the reactor. To consider an economic aspect of the reactor, STY was related to the applied amount of enzymes, thus resulting in a specific space-time yield (sSTY)(Eq. 13). For calculation of the sSTY the whole reactor volume was taken into account.

$$sSTY = \frac{\Delta C_{HK}}{\tau N_{Enzyme}} \quad (13)$$

3.3. Flow rate variation

As a first approach to validate the accuracy of the simulation model, variations of flow rate were analyzed computationally and experimentally (Figure 4). As expected, lower flow rates in the bioreactor led to an increase in the conversion rate due to a longer residence time of the substrate on the catalytic particle bed. Consequently, sSTY was increased for higher flow rates. In general, while theoretical prediction was almost identical to the experimentally determined value at the low flow rate (0.5 $\mu\text{L}/\text{min}$), the model slightly underestimated the conversion at higher flow rates (Figure 4B). These differences between experiment and simulation can be based on the fact that modeling of properties important for mass transfer limitation, such as diffusion coefficients, Sherwood correlation and porosity or tortuosity, differ from the real-world settings. This should particularly account for topological differences, such as inhomogeneities in the surface and layer thickness of the packed-bed,

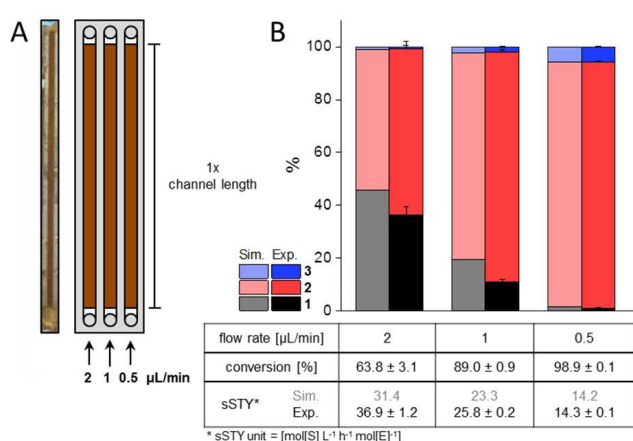


Figure 4. Variation of flow rates. A) Image and schematics of the microfluidic reactor filled with 4.5 mg Gre2-MBs leading to a 1x filled channel. B) Comparison of data obtained by theory (grey) and experiment (black). The bar diagram shows product distributions determined by HPLC analysis. The dimensions of the catalytic bed were held constant (1x channel length, 1x layer thickness).

as observed in confocal microscopy analysis of the bed (Figure S3). Since higher flow rates lead to increased sSTY values but also to decreased conversion rates (Figure 4), we limited the experiments to low flow rates of 0.5 $\mu\text{L}/\text{min}$ in order to optimize the reactor efficacy and conversion of the precious substrate 1.

3.4. Variation of packed-bed length

To further validate the mathematical model, we examined the effects of variable lengths of the packed-bed under constant flowrate conditions of 0.5 $\mu\text{L}/\text{min}$ (Figure 5). Since the experiments only allow for endpoint measurements at the end of the bed, the alteration of channel length should enable the verification of the model predictions regarding the precision of the implemented kinetic parameters and the resulting performance of the reactor system. To this end, the channel was filled with 4.5 mg of Gre2-MB leading to a bed length of 50 mm (defined as "1x" length). Accordingly, 2.25, 1.125 and 0.45 mg of Gre2-MB led to shorter bed lengths (0.5x, 0.25x and 0.1x, respectively; see Figure 5 A and Figure S3).

We found that the experimental data were in good agreement with mathematical simulations (Figure 5B). As expected, shortening of packed beds channels led to lower product yields, while sSTY values were increased. As predicted by simulation and verified by experiment, a 50% reduction of MB led to a 1.4-fold higher sSTY, whereas employment of only 10% of the catalytic MB led to a 2.2-fold increased sSTY. The increase in sSTY under decreased conversion can be explained by the decreasing substrate concentration over the bed's length. Thus, the data suggest that most of the reaction takes place at the front of the reaction bed where the substrate is present in high concentrations. Although the high sSTY observed for short beds indicates a high reactor efficiency, the use of this approach for

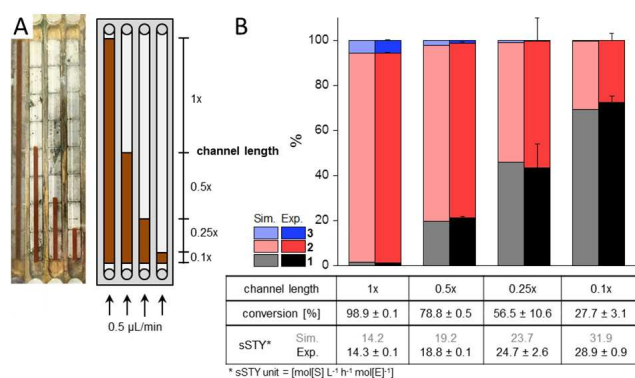


Figure 5. Flow reactor experiments with variable bed lengths. A) Image of flow channels filled with variable amounts of Gre2-MB and corresponding schematic depictions. B) Comparison of simulated (Sim.) and experimental (Exp.) data. Note that lower Gre2-MB loading led to lower product yields, as predicted by pre-experimental simulation data. However, sSTY can be significantly enhanced by shorter packed beds. Flow rate was held constant at 0.5 $\mu\text{L}/\text{min}$. The layer thickness of the catalytic bed was held constant (1x) whereas the channel length was varied between 1x and 0.1x (see text for details).

reducing the amount of catalytic materials is not practicable since only low total product conversion is achieved with the short beds.

So far we have only considered the dependence of substrate conversion and $sSTY$ on the flow rate (Figure 4) and the bed length (Figure 5) of the reactor determined at its outlet. However, the simulation data also allow a detailed consideration of the spatial distribution of the conversion rate and substrate concentrations within the entire reactor volume. Figure 6 illustrates the relation between substrate reduction, NADPH regeneration and diffusion of the reactants in the reactor space under steady-state conditions. As shown in Figure 6 A, the rate of reduction from 1 to 2 in the front upper part of the packed-bed is very fast. However, the reaction rate slows down in the direction of flow when the concentration of 1 decreases as a result of consumption (Figure 6B). The high reaction rate of the reduction is also associated by the high NADPH consumption in the front of the reactor bed. This results in a very low local concentration of the cofactor (Figure 6 C). After about 1/5 of the channel length, however, the regeneration reaction of the cofactor overcompensates its consumption so that the NADPH concentration rises again gradually.

Importantly, the spatial analysis indicates that reaction rates and concentrations of 1 and NADPH vary largely along the bed thickness (y-axis). Mass transport in y-axis only takes place by

diffusion and one might assume that catalytic entities further away from the upper boundary of the packed bed perceive lower substrate concentrations, thus leading to reduced reaction rates. However, the simulation shows that this is not true as the concentration of substrate 1 is almost constant over the y-axis of the entire reactor space (panel B). Therefore, the limitations of the reduction rate (panel A) most likely are due to the dependency on the availability of NADPH. Indeed, this is confirmed in panel C which shows that the regeneration process in the front regions of the reaction bed is not sufficiently effective to provide high concentrations of NADPH.

Both reduction reactions show the similar dependency on the available NADPH (Figure 6 A, Figure S14). However, as indicated by previous work^[13a,29] and the kinetic data in Table S3, the reaction rate of the second is significantly slower than that of the first reduction (1 to 2). Since 2 is produced inside the MB layer, the transfer rate from 2 to 3 is more evenly distributed (Figure S14).

Higher flow rates of 1 and 2 $\mu\text{L}/\text{min}$ were analyzed accordingly by simulation (Figure S15 and S16). Due to the increased flow rate, compounds are moving faster along the flow path, thereby reducing the residence time and the conversion rates. Hence, spatial distributions are stretched in flow direction.

Overall, Figure 6 nicely illustrates that a steady-state balance between substrate reduction and NADPH regeneration is established in the reactor, due to competing reactions of NADPH consumption and regeneration in V_{bed} and V_{ec} . An important result of this simulation is that the cofactor regeneration system is not optimal to meet the high cofactor demand in deeper regions of the porous bed. These observations emphasize the potential for optimization of the reactor system.

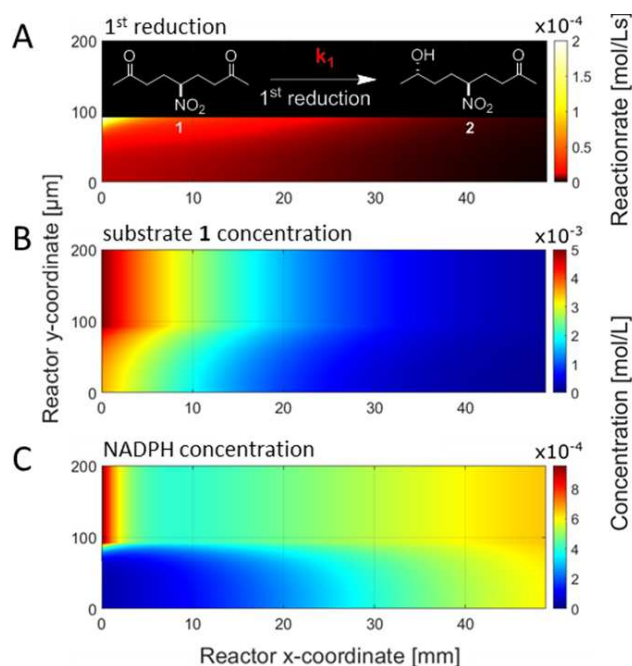


Figure 6. Simulated spatial distribution of reaction rates and reactant concentrations inside the microreactor. The simulation shows that A) high conversion rates for reduction of 1 to 2 occur in the front of the Gre2-MB packed-bed, thus leading to high consumption of NADPH (visualized in panel C). B) The distribution of educt 1 in the packed-bed, where it is reduced to 2, indicates a rapid decrease of 1 in flow direction. C) The high concentration of NADPH in the front of the reactor is immediately consumed by the reduction of 1 in the upper region of the bed. After almost complete conversion of 1, increased concentrations of NADPH occur due to regeneration by GDH. Simulated flow rate is 0.5 $\mu\text{L}/\text{min}$.

3.5. Variation of layer thickness

The validation of our mathematical model with altered flow rates (Figure 4) and channel lengths (Figure 5) of the reactor suggested that an improvement in reactor productivity could be achieved by varying the bed thickness. In particular, the spatial distribution of reaction rates and reactant concentrations indicated that areas of unused catalytic particles are located at the bottom of the packed bed (Figure 6). We therefore investigated whether a reduction of the packed bed's thickness would improve the reactor performance (Figure 7). To experimentally realize an altered bed thickness, a glass spacer was included between the

Nd magnets and the bottom of the bioreactor chip to weaken the magnetic field strength. Indeed, application of 1.125 mg MB into the channel resulted in an about 50% reduced layer thickness (0.5x), as compared to the standard thickness (see Figure 7 A and Figure S3 D).

Figure 7 shows a comparison of theoretical and experimental results depending on the dimensions of the packed bed. A reduced layer thickness leads to a larger volume above the packed bed, thereby reducing the flow velocity by about 30%

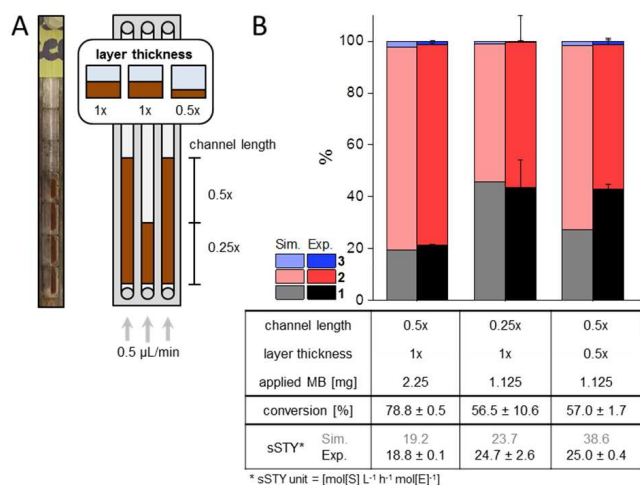


Figure 7. Influence of layer thickness and bed length. A) Image and schematics of the microfluidic reactor. The variable lengths and layer thicknesses were obtained by variation of the amount of Gre2-MBs and magnetic restraining forces (see text for details). B) Comparison of data obtained by theory (grey) and experiment (black). The bar diagram shows product distributions determined by HPLC analysis. The flow rate was held constant at 0.5 µL/min.

(i.e., from 77 to 54 µm/sec for 1× and 0.5× layer thickness, respectively) and increasing the residence time by 40% (from 319 to 453 sec for a 1× and 0.5× layer thickness, respectively) in the simulations. Comparison of calculated data and experimental results indicates that the model can predict the behavior of the reactor quite precisely. However, slight deviations occur in cases where identical amounts of catalytic beads are arranged in two different configurations (middle and right set of bars, in Figure 7B). It is expected that the short and thick bed (0.25x/1×, middle) will provide a lower conversion than the long and thin bed (0.5x/0.5×, right). Experimental data do not confirm this expectation, possibly, due to the above mentioned inhomogeneities of the packed bed, which are evident from microscopy analysis (Figure S3).

The data clearly indicate the validity of the overall prediction drawn from the simulated, spatial reaction rate and substance distributions within the microreactor (Figure 6). As indicated from the sSTY values, a thinner bed with the same length leads to a 30% increase in reactor efficiency (left and right set of bars, respectively, in Figure 7B). The reason for this is that the reduced layer thickness allows for improved availability of regenerated NADPH. However, it still cannot compensate the high cofactor demand in deeper layers of the porous bed. In fact, the catalytic bed holds a very high concentration of Gre2, which can be estimated as about 23.6 µM on average inside of the porous layer, whereas the NADPH diffusion from the overflowing 5 µM GDH solution is severely limiting the concentration of NADPH inside the layer (see Figure 6 C). This clearly shows that the equilibrium between the Gre2-catalyzed consumption and the GDH-mediated provision of NADPH needs to be adjusted. Indeed, simulations on the performance of reactors with variable bed thicknesses indicated that higher sSTY can be obtained by a

reduced layer thickness (Figure S17). This strategy can be implemented, for instance, by taking into account the development of thin-film reactors.^[8]

4. Conclusions

In summary, we have developed a novel mathematical reactor model, which is based on modular rate laws to simulate the behavior of a microfluidic packed bed reactor. The validity of the model was confirmed by experimental data regarding variations in process conditions (flow rate) and dimensions of the catalytic bed (length and thickness). We found a good agreement of the mathematical model and the experimental data. In fact, the modeling of experimental data made it possible to identify the critical parameter of the reactor format, which is layer thickness of the catalytic bed that limits the availability of the NADPH cofactor. Therefore, by adjusting the layer thickness, both the required amount of enzymatic catalyst could be reduced and the space-time yields of the reactor could be increased. While only a few data points could be taken into account here due to experimental limitations in the variation of the layer thickness, this approach should be useful for later studies on the packed bed or other formats, e.g. thin-film reactors. Hence, our results clearly show that the modeling of reactors for flow biocatalysis is a useful means to optimize process efficacy.

With the approach described in this paper, a complex reaction mechanism consisting of two interlinked enzymatic catalysis steps has been mapped for the first time. Further refinements of this approach will include, for example, the co-immobilization of the cofactor regeneration enzyme on the same MB as the KRED or by mixtures of different batches of MB bearing enzymes for cofactor regeneration and consumption. These are promising approaches with which such formats and similar microreactors can be optimized by means of modeling in order to contribute to the establishment of flow biocatalysis for technical applications.

Experimental Section

Experimental Details can be found in the Supporting Information. Abbreviation can be found in the Supporting Information.

Acknowledgements

This work was supported by Deutsche Forschungsgemeinschaft (DFG) through grant Ni399/15-1 and the Helmholtz programs 'Biointerfaces in Technology and Medicine' and 'Science and Technology of Nanosystems' and KIT Division I seed funding. We thank Christin Lederer for experimental help.

Conflict of Interest

The authors declare no conflict of interest.

Keywords: biocatalysis · enzyme immobilization · mathematical modeling · microreactor · stereoselective reaction

- [1] a) G. Schneider, *Nat. Rev. Drug Discovery* **2017**, *17*, 97; b) S. Chow, S. Liver, A. Nelson, *Nat Rev Chem* **2018**, *2*, 174–183.
- [2] a) B. P. Mason, K. E. Price, J. L. Steinbacher, A. R. Bogdan, D. T. McQuade, *Chem. Rev.* **2007**, *107*, 2300–2318; b) R. Wohlgemuth, I. Plazl, P. Znidarsic-Plazl, K. V. Gernaey, J. M. Woodley, *Trends Biotechnol.* **2015**, *33*, 302–314.
- [3] a) K. S. Rabe, J. Muller, M. Skoupi, C. M. Niemeyer, *Angew. Chem. Int. Ed. Engl.* **2017**, *56*, 13574–13589; b) J. Britton, S. Majumdar, G. A. Weiss, *Chem. Soc. Rev.* **2018**, *47*, 5891–5918; c) L. Tamborini, P. Fernandes, F. Paradisi, F. Molinari, *Trends Biotechnol.* **2017**, *36*, 73–88; d) J. H. Schrittwieser, S. Velikogne, M. Hall, W. Kroutil, *Chem. Rev.* **2018**, *118*, 270–348.
- [4] G. W. Huisman, J. Liang, A. Krebber, *Curr. Opin. Chem. Biol.* **2010**, *14*, 122–129.
- [5] T. Tyrikos-Ergas, V. Giannopoulos, I. Smonou, *Molecules* **2018**, *23*.
- [6] J. S. Carey, D. Laffan, C. Thomson, M. T. Williams, *Org. Biomol. Chem.* **2006**, *4*, 2337–2347.
- [7] D. Kim, A. E. Herr, *Biomicrofluidics* **2013**, *7*, 041501.
- [8] J. Britton, R. P. Dyer, S. Majumdar, C. L. Raston, G. A. Weiss, *Angew. Chem. Int. Ed. Engl.* **2017**, *56*, 2296–2301.
- [9] A. D. Keefe, D. S. Wilson, B. Seelig, J. W. Szostak, *Protein Expression Purif.* **2001**, *23*, 440–446.
- [10] B. Zakeri, J. O. Fierer, E. Celik, E. C. Chittock, U. Schwarz-Linek, V. T. Moy, M. Howarth, *Proc. Mont. Acad. Sci.* **2012**, *109*, E690–697.
- [11] A. Keppler, S. Gendreizig, T. Gronemeyer, H. Pick, H. Vogel, K. Johnsson, *Nat. Biotechnol.* **2003**, *21*, 86–89.
- [12] G. V. Los, L. P. Encell, M. G. McDougall, D. D. Hartzell, N. Karassina, C. Zimprich, M. G. Wood, R. Learish, R. F. Ohana, M. Urh, D. Simpson, J. Mendez, K. Zimmerman, P. Otto, G. Vidugiris, J. Zhu, A. Darzins, D. H. Klaubert, R. F. Bulleit, K. V. Wood, *ACS Chem. Biol.* **2008**, *3*, 373–382.
- [13] a) T. Peschke, M. Skoupi, T. Burgahn, S. Gallus, I. Ahmed, K. S. Rabe, C. M. Niemeyer, *ACS Catal.* **2017**, *7*, 7866–7872; b) T. Peschke, P. Bitterwolf, S. Hansen, J. Gasmı, K. S. Rabe, C. M. Niemeyer, *Catalysts* **2019**, *9*, 164;
- c) C. J. Hartley, C. C. Williams, J. A. Scoble, Q. I. Churches, A. North, N. G. French, T. Nebl, G. Coia, A. C. Warden, G. Simpson, A. R. Frazer, C. N. Jensen, N. J. Turner, C. Scott, *Nat Catal* **2019**.
- [14] C. Ruffert, *Micromachines* **2016**, *7*.
- [15] Y. Q. Lin, P. Yu, L. Q. Mao, *Analyst* **2015**, *140*, 3781–3787.
- [16] a) M. Serra, D. Ferraro, I. Pereiro, J. L. Viovy, S. Descroix, *Lab Chip* **2017**, *17*, 3979–3999; b) A. Dalili, E. Samiei, M. Hoorfar, *Analyst* **2019**, *144*, 87–113.
- [17] a) E. Gkantzou, M. Patila, H. Stamatis, *Catalysts* **2018**, *8*; b) D. B. Zheng, S. G. Wang, S. W. Qiu, J. Lin, X. J. Diao, *J. Biotechnol.* **2018**, *281*, 123–129.
- [18] L. Michaelis, M. M. Menten, *Biochem. Z.* **1913**, *49*, 333–369.
- [19] P. A. Saa, L. K. Nielsen, *Biotechnol. Adv.* **2017**, *35*, 981–1003.
- [20] M. D. Lilly, W. E. Hornby, E. M. Crook, *Biochem. J.* **1966**, *100*, 718.
- [21] D. Singh, S. Chaudhury, *ChemBioChem* **2018**, *19*, 842–850.
- [22] a) A. M. Al-Mayah, *Enzyme Res* **2012**, *2012*, 459190; b) W. R. Berendsen, A. Lapin, M. Reuss, *Chem. Eng. Sci.* **2007**, *62*, 2375–2385; c) P. Krause, G. Fieg, *Chem. Eng. Sci.* **2011**, *66*, 4838–4850.
- [23] W. Wibel, P. Ehrhard, *Heat Transfer Eng.* **2009**, *30*, 70–77.
- [24] M. Baerns, A. Behr, A. Brehm, J. Gmehling, H. Hofmann, U. Onken, *Technische Chemie*, Wiley-VCH, Weinheim, **2013**, p.
- [25] N. Kockmann, *Transport Phenomena in Micro Process Engineering*, Springer-Verlag Berlin Heidelberg, **2008**, p.
- [26] C. R. Wilke, P. Chang, *AIChE J.* **1955**, *1*, 264–270.
- [27] G. Emig, E. Klemm, *Chemische Reaktionstechnik*, Springer Vieweg, **2017**, p.
- [28] H. L. Weissberg, *J. Appl. Phys.* **1963**, *34*, 2636–2639.
- [29] M. Skoupi, C. Vaxelaire, C. Strohmann, M. Christmann, C. M. Niemeyer, *Chem. Eur. J.* **2015**, *21*, 8701–8705.
- [30] W. Liebermeister, J. Uhlendorf, E. Klipp, *Bioinformatics* **2010**, *26*, 1528–1534.
- [31] W. Liebermeister, E. Klipp, *Theor. Biol. Med. Modell.* **2006**, *3*.
- [32] G. E. Briggs, J. B. Haldane, *Biochem. J.* **1925**, *19*, 338–339.
- [33] P. C. Guo, Z. Z. Bao, X. X. Ma, Q. Xia, W. F. Li, *Biochim. Biophys. Acta* **2014**, *1844*, 1486–1492.
- [34] V. Kaswurm, W. Van Hecke, K. D. Kulbe, R. Ludwig, *Adv. Synth. Catal.* **2013**, *355*, 1709–1714.

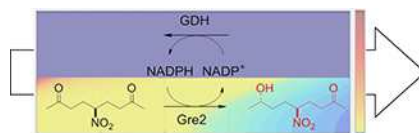
Manuscript received: January 27, 2020

Accepted manuscript online: February 3, 2020

Version of record online: ■■■, ■■■■

FULL PAPERS

Flow biocatalysis: Combination of mathematical simulations and experiments enable deeper insights and predictions regarding turnover and space-time yields of a microreactor for flow biocatalysis that employs two interconnected enzymatic transformations.



*T. Burgahn, P. Pietrek, Prof. R. Dittmeyer, Dr. K. S. Rabe, Prof. C. M. Niemeyer**

1 – 10

Evaluation of a Microreactor for Flow Biocatalysis by Combined Theory and Experiment

